

Micron-scale additive manufacturing of binary and ternary alloys by electrohydrodynamic redox 3D printing

Nikolaus Porenta ^{a,1}, Mirco Nydegger ^{a,1}, Maxence Men  trety ^a, Souzan Hammadi ^{a,b},
Alain Reiser ^{a,c}, Ralph Spolenak ^{a,*}

^a Laboratory for Nanometallurgy, Department of Materials, ETH Z  rich, Vladimir-Prelog-Weg 1-5/10, Z  rich 8093, Switzerland

^b Structural Chemistry Division, Department of Chemistry,   ngstr  m Laboratory, Uppsala University, 75120 Uppsala, Sweden

^c Department of Materials Science and Engineering, Massachusetts Institute of Technology, MA-02139 Cambridge, United States of America

ARTICLE INFO

Keywords:

Microscale
Nanoscale
3D printing
Alloys
Copper
Silver
Zinc
Metal
3D nanofabrication

ABSTRACT

Across disciplines and length scales, alloying of metals is a common and necessary strategy to optimise materials performance. While the manufacturing of alloys in bulk and thin film form is well understood, the fabrication of alloyed 3D nanostructures with precise control over the composition remains a challenge. Herein, we demonstrate that electrohydrodynamic redox 3D printing from mixed metal salt solutions is a versatile approach for the 3D nanofabrication of alloys. We propose that the droplet-by-droplet nature of the electrohydrodynamic redox printing process allows straightforward electroplating of alloys with composition solely controlled by the composition of the electrolyte solution, independent of the reduction potential of the involved cations. As a demonstration of the direct control of composition, we deposit binary and ternary alloys of Ag, Cu and Zn. TEM microstructure analysis indicates homogeneous alloying at the nanoscale and the formation of a metastable solid-solution phase for Ag-Cu and a two phase system for Ag-Cu-Zn alloys. The straightforward approach to alloying with an electrochemical technique promises novel opportunities for optimisation of properties of 3D nanofabricated metals.

1. Introduction

Additive manufacturing (AM) of metals at the micron-scale has received significant interest in recent years for its capability to produce three dimensional geometries that cannot be obtained by lithographic microfabrication techniques [1]. 3D structures of high geometric complexity or high aspect ratio are promising for applications in microelectromechanical systems [2], sensing [3], lab-on-a-chip applications [4], and mechanical metamaterials [5]. Yet, for AM to make an impact in microfabrication, technologies need to provide materials with properties appropriate for a diverse range of applications. In the case of metals, alloys rather than pure metals are often desired because of their improved properties, e.g. better mechanical [6,7], catalytic [8], or plasmonic [9] performance, or higher resistance to electromigration [10].

However, the integration of alloys into additively manufactured devices poses a challenge to small-scale AM. Currently, no technique offers a wide range of alloy compositions in combination with a high density and thus excellent mechanical performance (e.g. high strength) of

the deposited metals. Techniques based on sintering of inks containing metal, metal-oxide or metal salt particles offer in principle a wide range of materials and alloys [11] (for alloys, either alloyed particles or blends of elemental particles can be used). Similarly, the sintering of polymer structures (written with a laser) containing metal ions offers a versatile approach to small-scale AM, allowing high freedom in design [12]. However, the thermal post-print processing required to sinter the particles or to reduce the metal ions to a metallic state [13] renders these approaches incompatible with low-melting-point substrates. More critically, the sintered materials often contain residual porosity which lowers their performance [14] and significant shrinkage can lead to failure [15,16]. As with ink-based AM, porosity is also a major challenge for materials deposited by laser induced forward transfer (LIFT) of molten metal thin films [14], even though the approach offers high flexibility to tune the composition (for example, Ag-Cu [17], Ni-Cr, Zr-Pd [18] and Ni-Ti [19,20] have been demonstrated). Focused electron beam induced deposition (FEED) allows fabrication of alloyed struc-

* Corresponding author.

E-mail address: ralph.spolenak@mat.ethz.ch (R. Spolenak).

¹ These authors contributed equally.

tures as well [21,22], namely by using multiple gas injection systems [23,24] or the use of multi-metal precursors [25]. However, the often high carbon content in the structures also requires a post-processing step to achieve high metal purity. In contrast, electrochemical AM (ECAM) techniques fabricate as-printed dense and pure metal structures from a wide range of readily available metal salt precursors [26–31], and are thus promising candidates for the direct deposition of high-performance materials. In general, a wide range of alloys can be electroplated in thin-film form [32] and should, in principle, be accessible with small-scale ECAM as well – yet, only recently a number of binary alloys have been demonstrated: Cu–Co alloys with variable composition by meniscus confined deposition [33], Ni–Co and Ni–Mn alloys by electroplating of locally dispensed ions (FluidFM) [34] and Cu–Ag alloys by electrohydrodynamic redox printing (EHD-RP) [35]. A general challenge in the deposition of alloys is the retardation of the more noble metal's deposition rate to avoid its preferential deposition [32], which is typically achieved by a large surplus of the less noble metal ions [36], by the use of surface active additives [34,36,37], complexing agents, or deposition in diffusion limited current ranges [32]. Intriguingly though, spatially confined electrosynthesis offers a novel route towards chemically complex metal particles [38]. The previously reported deposition of Cu–Ag alloys by EHD-RP indicated that this technique can employ such a confined deposition to directly fabricate 3D alloys without the need of elaborate tailoring of the plating bath – significantly simplifying alloying by electrochemical deposition.

EHD-RP utilizes spatially confined electroplating to fabricate as-printed dense alloys. The technique is based on a solvent-filled quartz nozzle in close proximity (approx. 10 µm) to a conductive substrate. In its original setup, metal ions are generated *in-situ* from a sacrificial metal anode and attracted towards the tip of the printing nozzle by an applied potential between the anode and the substrate. Ion-loaded droplets are then ejected by electrohydrodynamic forces. Upon impingement of these droplets on the substrate, metal ions are reduced to elemental metal by charge-transfer from the substrate, while the solvent evaporates (both, organic and aqueous solvents have been demonstrated [35,39]). This allows for the additive manufacturing of small-scale three dimensional metal structures with a feature size of 150 nm. Deposition of intricate 3D shapes is not straightforward in EHD-RP due to the nature of the involved electric fields [40]. It is possible, however, to correct for electric field aberrations based on simulations and fabricate structures such as double helices, branched trees and stylised micro-bicycles. Furthermore, modulating the applied potential allows for a tuning of the microstructure [41]. For multi-metal deposition and alloy printing, EHD-RP has previously utilised double-channel nozzles [35], with each channel containing an elemental metal wire (demonstrated only for Cu and Ag). In such a setup, each metal ion species can be generated independently for depositing pure metals or simultaneously to deposit an alloy. This approach, however, did not allow for any control over the chemical composition and was only demonstrated for binary alloys.

In this paper, we demonstrate that the use of aqueous metal salt solutions instead of sacrificial metal anodes as ion sources in EHD-RP unlocks the deposition of binary and ternary alloys with tightly controlled compositions that span the whole composition space. To minimise the complexity of the fabrication process, micro-pillars were chosen as a model system, though arrays of micro-pillars have shown possible applications as surface enhanced Raman substrates [42] or to study interactions with living materials [43]. This approach therefore combines the complimentary benefits of different ECAM techniques, namely the large range of accessible metals (a large range of metal salts can be easily dissolved and deposited in aqueous solvents) with the indifference of the electrohydrodynamic ejection process towards the reduction potential of different cations. Furthermore, EHD-RP has been shown to exhibit high printing speeds (>10 voxel·s^{−1}) [1] and can be parallelised to further increase printing efficiency [44]. Therefore, it uniquely allows straightforward co-deposition of elements with strongly

different reduction potential such as Cu, Ag and Zn. This novel approach to micron-scale electrodeposition will facilitate expanding the accessible alloy space for small-scale AM.

2. Materials and methods

2.1. Solution preparation

For the preparation of aqueous metal salt solutions CuSO₄·5 H₂O (Sigma Aldrich, 99.999% metal basis), CuCl₂·2 H₂O (Sigma Aldrich, 99.999% metal basis), Ag₂SO₄ (Alfa Aesar, 99.999% metal basis), ZnSO₄·7 H₂O (Sigma Aldrich, 99.5% metal basis) and ZnCl₂ (Alfa Aesar, 99.995% metal basis) were used as received. Before use, the ZnSO₄·7 H₂O was dried at 130 °C for 2 h (Thermofisher Scientific, Herarus) to obtain ZnSO₄·H₂O. All glasswares used in following steps were cleaned by sonicating (Bandelin, SONOREX™) for a minimum of 15 min in ethanol (Supelco, Reag. Ph Eur) and subsequently high purity water (Fisher Chemical, Optima® LC/MS, used throughout this work). To prepare solutions with total metal ion concentrations of 1 mM and below, first 4 mM stock solutions were prepared by weighing in the corresponding amount of metal salt and dissolving it in high purity water. These solutions were then further diluted to prepare solutions used for printing. Solutions with a metal ion concentration of 10 mM were prepared directly from the metal salts.

2.2. Preparation and procedure for printing

Substrates used for printing were Au thin films on wafers. Si₃N₄ terminated Si-wafers (SiMat) were coated with a 5 nm Ti (Mateck, 99.995%) adhesion layer and 65 nm of Au (Mateck, 99.99%) using DC magnetron sputtering (PVD Products Inc.) at 250 W and 3 mTorr. These wafers were then covered with a protective layer (MRPL-40, Microresist) before dicing into 1.4 x 0.4 cm² large pieces using a wafer dicing saw (Disco DAD 3221). The protective layer was removed prior to use by sonication for 5 min in acetone and isopropanol.

Au-wires (Alfa Aesar, Premion®, 99.999% metal basis) were employed as anodes. Before use, they were cleaned in conc. HNO₃ (Sigma Aldrich) for 20 s and then thoroughly rinsed with high purity water (Fisher Chemical, Optima® LC/MS).

Nozzles with openings of approx. 130 nm were fabricated from quartz capillaries (Sutter Instruments, Item QF100-70-15) using a laser-based micropipette puller system (Sutter Instruments, P-2000) with similar parameters reported in previous literature [35]. Nozzles were filled with metal salt solutions using sterile syringes (BD, 5 mL Syringe Luer-Lok™ Tip) and needles (B. Braun, Sterican® 0.50 x 40 mm). Prior to use, the nozzles were rinsed with the metal salt solutions. The Au wire was then submerged in the filled nozzle and mounted onto the printing setup. Details of the printing setup used in this work have been described previously [35].

2.3. Analysis

Scanning electron microscopy (SEM) was conducted using a Magellan 400 (Thermo Fisher Scientific) equipped with an Octane Super (EDAX) energy dispersive x-ray (EDX) spectroscopy detector. All micrographs were acquired in the in-lens mode at a tilt angle of 55°, an acceleration voltage of 5 kV and a beam current of 25 pA. Micrographs are shown without tilt correction. TEM lamellas were prepared on a dual-beam Helios 5UX (Thermo Fisher Scientific, Ga⁺ liquid metal ion source). Prior to FIB-milling, the pillars were coated with a protective carbon layer by e-beam deposition. Scanning transmission electron microscopy (STEM) and transmission electron microscopy (TEM) were conducted on a Talos F200X (Thermo Fisher Scientific) operated at 200 kV. Inductively coupled plasma optical emission spectroscopy (ICP-OES) was performed on an ARCOS FHS12 system (Spectro).

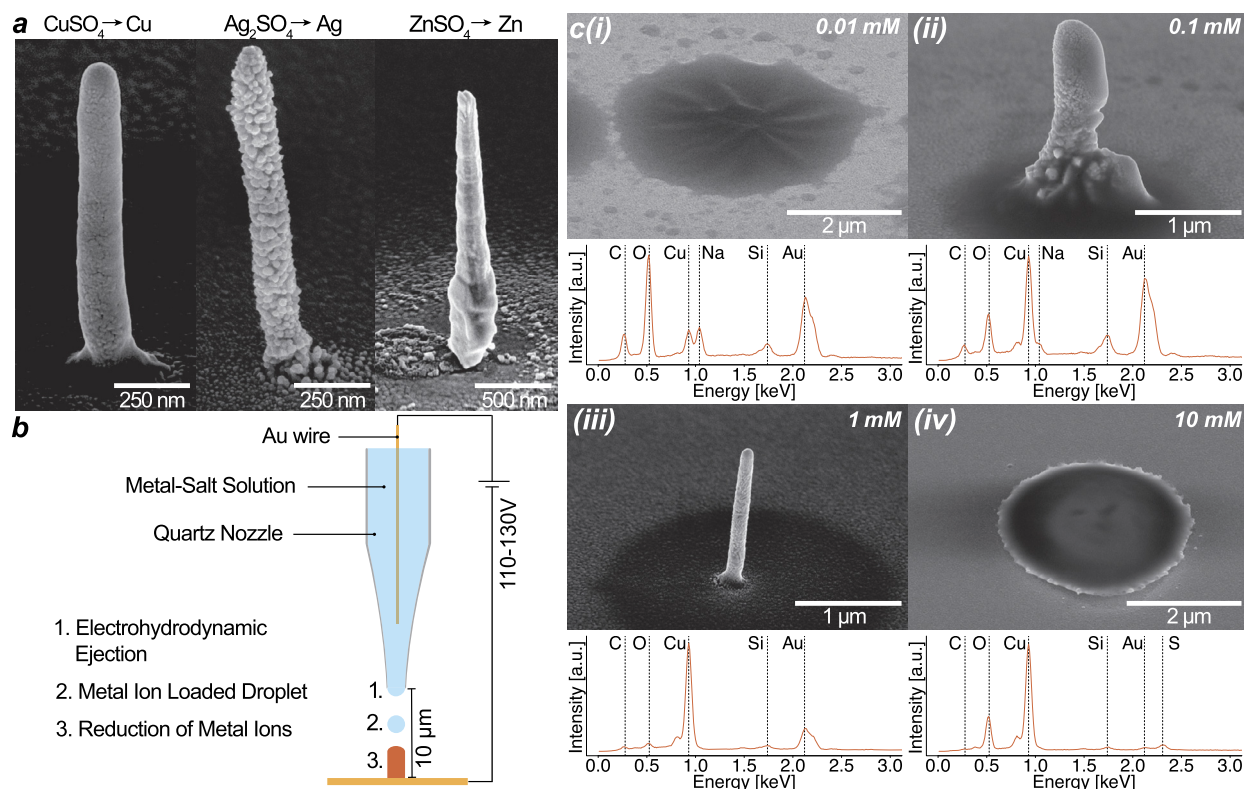


Fig. 1. Electrohydrodynamic redox-printing (EHD-RP) using metal salt solutions. (a) Cu, Ag and Zn structures deposited from the corresponding metal sulphate solutions. (b) Schematic of the experimental setup. A quartz capillary filled with an aqueous metal salt solution, is brought into close proximity (approx. 10 μm) of a conductive substrate. An electric potential (110–130 V) applied between an Au wire submerged in the solution and the substrate induces electrohydrodynamic ejection of cation-loaded droplets. Metal ions contained in the droplet are reduced to elemental metal upon impingement on the conductive substrate. (c) Secondary electron (SE) micrographs and EDX spectra of Cu structures printed from CuSO_4 salt solutions at concentrations of (i) 0.01, (ii) 0.1, (iii) 1 and (iv) 10 mM respectively. Confined Cu structures were obtained when printed from a 1 mM CuSO_4 solution. Lower concentrations caused C-, O- and Na-rich deposits. In contrast, a 10 mM solution led to the formation of broad, planar deposits rich in oxygen and sulphur.

Data analysis and plotting was done using RStudio: Integrated Development Environment for R (Version 2022.7.2.554). Means and standard deviations of elemental compositions were calculated from at least 4 measured values. For determination of the cell parameter a , d -values for five different diffraction rings were calculated from measured distances in diffraction space. These values were then used to determine an averaged a .

3. Results and discussion

3.1. Aqueous salt solutions as metal ion sources for EHD-RP

Cu, Ag and Zn pillars were printed using aqueous CuSO_4 , Ag_2SO_4 and ZnSO_4 solutions as ion sources (Fig. 1a). These metals were chosen to allow representative immiscible (Cu-Ag) and miscible (Cu-Zn) alloy systems. The phase diagram for Cu-Ag [45,46] shows a miscibility gap over the entire compositional range beneath approximately 300 $^\circ\text{C}$. The Cu-Zn phase diagram [47,48] exhibits 3 different intermetallic phases at 300 $^\circ\text{C}$. Pillars of different metals exhibited a different surface morphology. Cu formed a smooth surface consisting of small grains. The Ag pillars showed a much rougher surface with larger grains, though both Cu and Ag pillars had a constant diameter of approximately 150 nm. The diameter of the shown Zn pillar was about 315 nm at its base and about 120 nm at its apex. Zn pillars displayed a smooth surface, with some exhibiting a plate-like structure (for example visible for the shown pillar at the top). All structures showed only small amounts of contaminants (such as C and O) in Energy-dispersive X-ray spectroscopy (EDX) (Fig. S1), similar to previous demonstrations with sacrificial anodes [35,41]. While pillar diameters are comparable to previous reported values (Cu

pillars deposited with acetonitrile as a solvent were reported to have a diameter of 120 nm [35]), other geometric properties of the structures such as maximal aspect ratio have not been systematically investigated during this study.

Our results demonstrate the deposition of metallic structures with EHD-RP from aqueous metal salt solutions with similar characteristics to those previously printed from sacrificial anodes [35,39,41]. The general advantage in the use of metal salts over sacrificial anodes is the increased range of printable metals, because no anodic dissolution must be guaranteed (which can be a challenge, as shown for the case of Zn [39]) and soluble salts exist for a large variety of metals.

In contrast to the previous work with EHD-RP where only cations were generated *in-situ* from a sacrificial anode, the use of aqueous salt solutions entails the presence of anions in the solution as well. In principle, for fully dissociated salts, the electric field between the anode and the substrate will cause cations to migrate towards the orifice of the nozzle, while the anions migrate preferentially towards the anode. This separation should therefore allow for the ejection of cation-only loaded solvent droplets (Fig. 1b).

The concentration of the salt solutions is an important parameter for the deposition of pure metal structures (Fig. 1c). An optimal concentration of 1 mM CuSO_4 allowed for the deposition of high-purity and confined Cu structures (Fig. 1c(iii)). Here, co-deposition of the counter-ion can be excluded, since no S was detected with post-deposition EDX analysis. A lower concentration of 0.1 mM also led to the deposition of Cu (Fig. 1c(ii)), however, with a significantly increased amount of impurities, such as C, O and Na. When the concentration was further decreased to 0.01 mM, no out-of-plane deposition of Cu was observed (Fig. 1c(i)). Instead, patch-like deposits of C, O and Na with only a

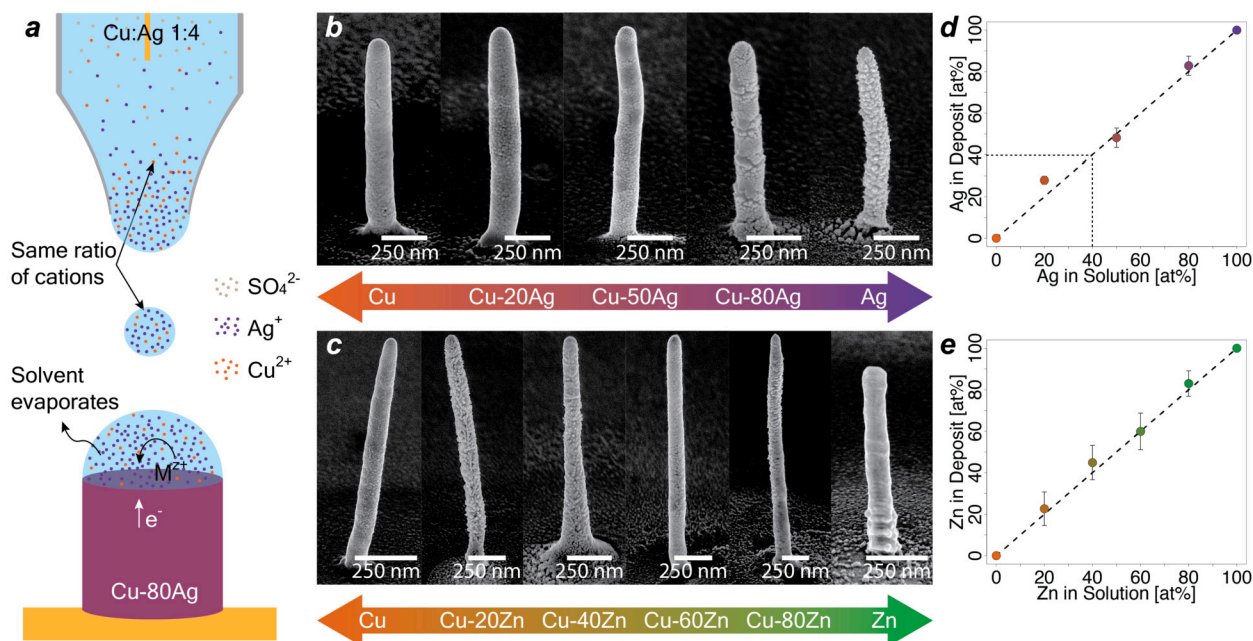


Fig. 2. Deposition of alloys from mixed solutions. (a) Schematic of the deposition process in EHD-RP. A droplet containing two species of solvated metal-ions, in the same ratio as in the solution, is ejected towards the substrate. There, the confined deposition in the droplet will lead to a structure with the same ratio of the metals as in the solution. (b) SE micrographs of pillars fabricated from aqueous sulphate solutions of varying Cu:Ag ratio (total metal ion concentration of 1 mM). From left to right the solution composition was pure Cu, Cu-20Ag, Cu-50Ag, Cu-80Ag and pure Ag. Surface roughness increases with Ag content. (c) SE micrographs of pillars fabricated from aqueous sulphate solutions of varying Cu:Zn ratio (total metal ion concentration of 1 mM). From left to right the solution composition was pure Cu, Cu-20Zn, Cu-40Zn, Cu-60Zn, Cu-80Zn and pure Zn. (d, e) Ag and Zn content in the deposited structures as determined by Energy-dispersive X-ray spectroscopy (EDX) plotted versus their nominal content of the respective printing solutions. For both, Cu-Ag (d) and Cu-Zn (e), the composition of the printed structures is identical with the ratio of metal ions in the printing solutions.

low amount of Cu were formed. A CuSO_4 concentration of 10 mM decreased the quality of deposited structures as well (Fig. 1c(iv)). Notably, no confined out-of-plane growth was possible at these concentrations. The resulting broad, disk-like structures contained significantly more O and also contained S. Similar results were found for CuCl_2 salt solutions (Fig. S2). Cl-rich deposits were deposited when using a concentration of 10 mM CuCl_2 . For structures printed using 1 and 0.1 mM CuCl_2 solutions, the level of O and C impurities were comparable, indicating a broader useful concentration range. Nevertheless, sulphate salts were chosen for subsequent alloying studies due to their better solubility in water, e.g. 30 mM for Ag_2SO_4 compared to 0.001 mM for AgCl [49]. The printing voltage used during deposition were 136, 137, 127 and 130 V for the 0.01, 0.1, 1 and 10 mM CuSO_4 solutions respectively.

We hypothesise that the purity of the deposits printed from electrolytes of low concentration is closely related to the ratio of Cu ions to other non-volatile species present in the solvent (such as Na or large organic molecules). The results suggest that if a diluted metal salt solution is used, less metal ions are present in ejected droplets compared to a constant amount of contaminant species, leading to a large amount of contaminants incorporated in the structure. For example, EDX measurements indicated a roughly seven times increase of Na contamination when printing with a ten times lower CuSO_4 concentration (the deviation of the expected 10 fold increase of Na could be caused by the fact that EDX measurements on light elements exhibit larger errors, therefore the observed deviation might stem from measurement inaccuracies).

At high electrolyte concentrations of 10 mM, deposition is non-confined and contaminated. In the case of sulphate salts, the presence of S and the higher O content in these structures indicate that the sulphate-anions started to be co-deposited. Similarly, Cl was found in deposits printed with CuCl_2 . This indicates that electrohydrodynamic ejection is not sufficiently selective at these concentrations. As described above, in an ideal case, all negatively charged species would migrate towards the anode and are not ejected from the nozzle. However, at high salt

concentrations, this ideal situation appears to break down. One reason could be the formation of positively charged complexes containing anions. It is known that in an aqueous solution of Cu^{2+} and Cl^- , a fraction of the Cu(II) ions are present as $[\text{Cu}(\text{II})\text{Cl}]^+$ complexes even at concentrations as low as 10 mM [50]. Such complexes are still positively charged, therefore attracted towards the tip of the nozzle and ejected. In summary, our data indicate that a salt concentration of 1 mM is a midpoint between high contamination levels and the co-deposition of anions. A finer concentration sweep could potentially help to further optimise purity, but was not conducted as part of this study.

Another significant difference between the two approaches (dissolved metal salts and sacrificial anodes) is how the charge neutrality of the process is established. For sacrificial anodes, the dissolution of the anode balances the electrons necessary for the reduction on the substrate [35]. For metal salt solutions, however, a different oxidation reaction must take place at the anode (given that the element of the anode, Au, was never found in structures printed on various substrates). Due to the low concentration of anions in the solution we expect the oxidation of water to oxygen and H^+ to take place at the anode.

In general, the distinct surface morphologies of the different metals printed for this work are in agreement with previous work that employed sacrificial anodes as ion sources [35]. Minor differences can be attributed to the fact that the morphology is a sensitive function of the deposition potential [41], but presumably also of the presence of contaminants and nozzle shape. Since the variations in surface morphology observed during this work are within the variations we observed with sacrificial anodes, we conclude that the use of aqueous metal salt solutions does not significantly affect the morphology of fabricated structures.

3.2. Deposition of binary alloys

Binary Cu-Ag and Cu-Zn alloys with compositions spanning the complete composition space were deposited from mixtures of the respective

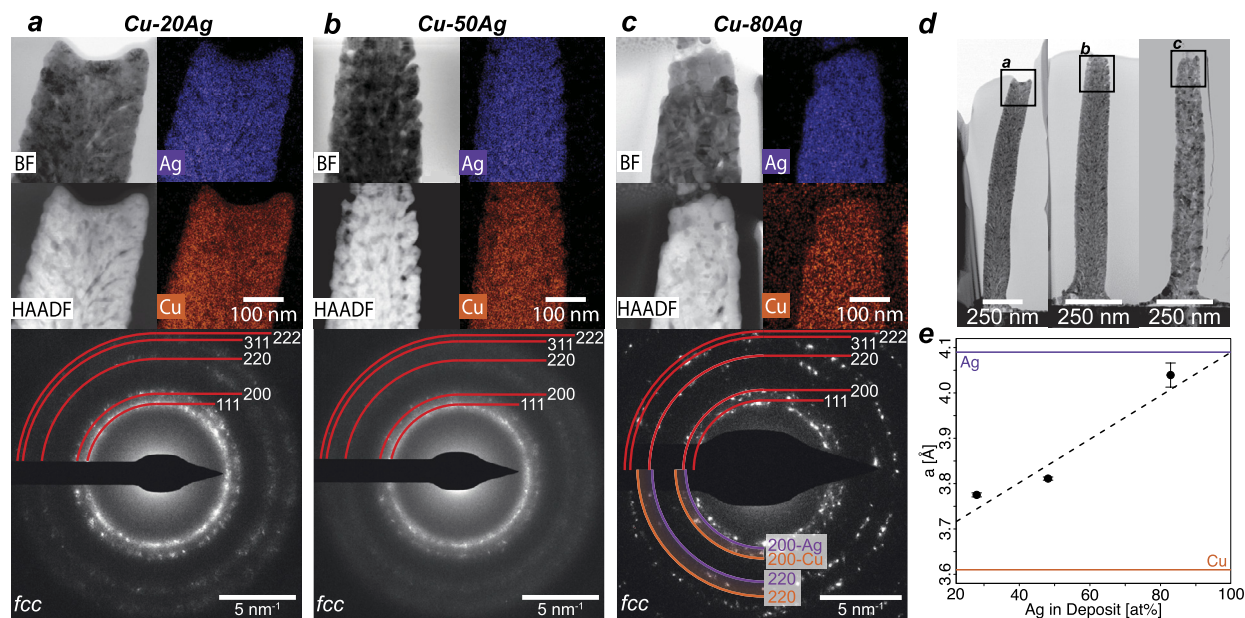


Fig. 3. Microstructure of Cu-Ag alloys. (a–c) STEM brightfield (BF) and high-angle annular darkfield (HAADF) micrographs of thinned Cu-20Ag, Cu-50Ag and Cu-80Ag (nominal concentration) pillars respectively, with the corresponding Ag and Cu EDX elemental maps as well as selected area electron diffractograms, acquired in the middle of the pillars. The EDX maps indicate the presence of a single phase rather than two separated phases as would be expected for Cu-Ag alloys (in thermodynamic equilibrium). Correspondingly, electron diffractograms show only a single set of diffraction rings, indicating a single phase fcc system. The purple and orange lines in the diffraction pattern of Cu-80Ag indicate where the 200 and 220 reflexes of the respective pure metal would be expected (indeed, no reflexes for the pure Ag and Cu phases are found). However, as for the 200 reflections, they are also not exactly on the same arch. Consequently, there is either a different stress state from grain to grain or a slightly different composition, indicating partial phase separation into Cu- and Ag-rich grains. (d) low magnification images of the pillars used to study the microstructure. (e) The lattice parameter a (as determined from electron diffraction patterns) vs. the measured Ag content (at-%). The violet and orange lines indicate the lattice parameter for pure Ag and Cu respectively, while the dashed line plots the expected values of a for a solid solution according to Vegard's law.

metal salt solutions (total metal ion concentrations of 1 mM). For the sake of simplicity, we refer to all alloys as Cu based (e.g. Cu-80Ag for an alloy with a nominal composition of 20 at% Cu and 80 at% Ag). The composition of the electrodeposited structures could directly and precisely be adjusted simply by tuning the metal-cation ratio of the electrolyte mixtures accordingly. The atomic composition of the printed structures, determined by EDX in post-deposition, mirrored the concentration of the corresponding metal-ions in solution (Fig. 2d–e). EDX measurements were performed in a TEM in the case of Cu-Ag (d) and an SEM in the case of Cu-Zn (e), hence the larger error bars for the Cu-Zn samples. The composition of the electrolyte mixtures was validated using inductively coupled plasma optical emission spectroscopy (ICP-OES) (Tab. S1).

The capability of direct and exact compositional control most likely stems from the ejection of all cations present in solution irrespective of the species. Fig. 2a illustrates a schematic of the deposition process. The solvent droplets, ejected from the nozzle towards the substrate, carry the same ratio of solvated metal ions as the electrolyte solution. Note that the charge of the ions seemed to be irrelevant, as Ag ions are singly charged while Cu and Zn are (in aqueous solutions) doubly charged. Once both species are ejected according to the designed ratio, the translation from droplet composition into alloy composition upon reduction is inevitable. We argue that no matter the fundamental details of this process, the alloy deposition will always mirror the composition of the droplet. Previous work on EHD-RP suggests that two fundamentally different growth scenarios are possible [41]. In the first scenario (observed at low printing voltages and thus low solvent flow rates), it is assumed that an arriving droplet dries before impingement of a next droplet. In the second scenario, higher flow rates balance evaporation rate and enable a constant coverage of the growth interface with a stationary solvent droplet. Both options should lead to deposition of an alloy with the intended chemical composition. In case of transient droplets, the complete evaporation forces the deposition of all metal ions. In case

of a stationary droplet, the different reduction potentials might lead to preferential deposition of the more noble species at first. Nonetheless, even if this is the case, the build-up of less noble cation would increase its deposition rate, eventually reaching a steady state where the ratio deposited is equal to the ratio of incoming metal ions.

The demonstrated control of composition is a significant advancement compared to previous alloying attempts with the EHD-RP method [35], where no control over the composition was achieved and where only an alloy of roughly a composition of 1:1 could be deposited. Yet, many potential applications for alloys demand precise compositional control to achieve the desired properties. For example, the optical properties of noble metal alloys, such as Cu-Ag, depend strongly on their elemental ratio [9]. To increase the corrosion resistance of Cu structures only low amounts of added Ag are necessary [51]. A further possible application of binary alloys with well defined compositions is the fabrication of nanoporous metal structures with tuned ligament sizes and volume fraction [52]. Exerting precise control over these parameters enables the manipulation of material properties, such as mechanical [53] or optical [54] characteristics. Therefore, the straightforward control of composition merely through setting the appropriate ratio in the electrolyte of EHD-RP promises a high versatility of the technique.

In line with observations for pure metals, the surface morphology of the deposited alloys is a function of their chemical composition. In the Cu-Ag alloy for example, surface roughness increased with a Ag content >50 at% (Fig. 2b). Similarly, a high Zn content in Cu-Zn alloys led to a plate-like surface (Fig. 2c). Structures with a Zn content of 20 at% and 40 at% had increased surface roughness compared to pure Cu, but not in a plate-like manner – yet it is currently unclear whether this increase in roughness is related to the composition alone or also deposition parameters. This change in surface morphology with different metal compositions could be used to deposit structures with designed surface morphologies. However, a more detailed investigation has to be conducted to better understand these morphological changes.

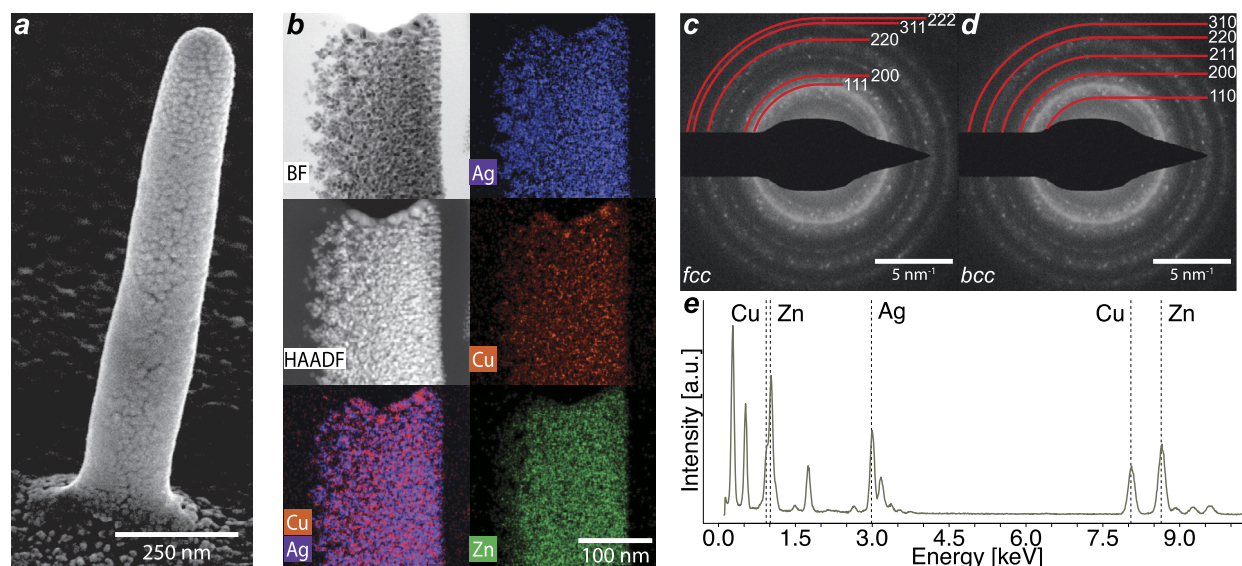


Fig. 4. Deposition of a ternary Cu-Ag-Zn alloy. (a) SEM micrograph of a Cu-33Ag33Zn alloy printed from an equimolar Cu, Ag and Zn sulphate solution (total metal ion concentration of 1 mM). (b) STEM bright-field micrograph of a cross-section of a pillar with corresponding Ag, Cu and Zn EDX maps. (c) Selected area electron diffractogram of the same pillar overlaid with an fcc pattern, as expected for pure Ag and Cu phases. (d) The same selected area electron diffractogram overlaid with a bcc pattern, as expected for Zn-containing intermetallic phases. Both patterns, fcc and bcc, fit some diffraction rings, indicating an at least two phase system. (e) EDX spectrum of the same alloy. The main peaks of interest are marked, while further peaks (C, 0.277 keV; O, 0.525 keV; Ga, 1.098, 9.241 keV; Al, 1.486 keV; Si, 1.739 keV and Mo, 2.623 keV) arise from the substrate, specimen preparation or the TEM instrument itself.

Fig. 3a-c shows TEM micrographs of the microstructure as well as electron diffraction patterns of thinned pillars of Cu-20Ag, Cu-50Ag and Cu-80Ag respectively. The micrographs revealed variations in grain structure between the different samples, which could be related either to changes in composition, printing voltage or concentration of contaminants [41]. EDX elemental maps in all three cases showed homogeneous spatial distribution of both Cu and Ag (for EDX spectra see Fig. S3). For Cu-20Ag and Cu-50Ag, only a single, but diffuse set of fcc diffraction rings was found, indicating a single solid-solution phase. Cu-80Ag showed more distinct reflexes, consistent with the observed larger grain size. The same reflexes were not located precisely on the same arc, but spread between the arcs expected for pure Cu and Ag respectively. The measured lattice parameters are in good agreement with values calculated for solid solutions according to Vegard's law [55] (Fig. 3d). The lattice parameters were averaged from the d-spacings of the five different diffraction rings, each measured at the most intense part of the rings. Note that other techniques, such as X-ray diffraction, are not suitable to determine the lattice constant for these samples, as the volume of printed material is too small for reliable measurements. Further experiments showed that phase separation can be induced by annealing at 150 °C for 1 h (Fig. S4).

In general, Cu-Ag alloys are expected to form a phase-separated microstructure at the thermodynamic equilibrium, as Cu and Ag are immiscible over a wide range of compositions [46]. In our case, EDX and diffraction data suggest limited phase separation or even a single fcc Cu-Ag phase for all compositions. Similar microstructures have been reported for Cu-Ag alloys fabricated in a kinetically controlled regime [56,57]. This indicates the deposition in EHD-RP is also kinetically dominated. As a matter of fact, our current densities and, accordingly, deposition rates are very high compared to other electrochemical processes. In EHD-RP, current densities are typically 2–20 A/cm² (a typical deposition current for EHD-RP is between 5·10⁻⁹ to 5·10⁻¹⁰ A, while the horizontal cross-sectional area is about 0.018 µm²). These numbers are up to 1000 times higher than for standard electrodeposition processes of alloys [58–60]. Hence, the use of phase diagrams to predict the phases of deposited alloys is hindered by the highly dynamic, non-equilibrium state in which the deposition takes place.

3.3. Fabrication of Cu-Ag-Zn ternary alloy

A mixed, equimolar electrolyte of Cu, Ag and Zn sulphate extended the number of alloying elements that can be co-deposited (Fig. 4a). The phase diagram of this ternary system has been studied in literature [61, 62]. It has been shown to form complex multi-phase systems, especially for Zn contents >30 at%. Again, the composition of the printed alloy closely mirrored the composition of the solution (nominal composition of 33.3 at% of each component): 35.1 ± 2.8 at% Ag, 28.9 ± 2.0 at% Cu and 36 ± 2.1 at% Zn (as determined by EDX spectroscopy in TEM, Fig. 4e). The printed Cu-Ag-Zn structure exhibited very small grain size of approx. 10 nm (Fig. 4b), and probably featured some intergranular nanoporosity. EDX maps indicated that the distribution of the elements is less homogeneous than in the binary alloy, however, with variations only at the same length scale as the grain size.

The observed diffraction pattern is characteristic of both an fcc phase and a body-centered-cubic (bcc) phase (Fig. 4c-d). A hexagonal-close-packed (hcp) pattern, as would be expected for pure Zn, is not found in the observed pattern (Fig. S5b). The diffraction rings corresponding to an fcc phase appear diffuse and are broad, similar to those in (Fig. 3a-b). Again, such broad rings could be due to partial phase separation into Cu- and Ag-rich grains or dissimilar stress states. The sharper diffraction rings could originate from a bcc phase, as expected for Zn-containing intermetallic phases. The presence of such a Zn-rich phase would fit well with the EDX elemental maps. This explanation is in agreement with literature, where for an equimolar Cu-Ag-Zn alloy at the thermodynamic equilibrium a three phase system was observed [61,62] (two fcc phases and a bcc phase). The two fcc phases should correspond to a Cu-rich/Ag-poor and Ag-rich/Cu-poor phase respectively. Both these phases will have a significant Zn content (>13at%). The bcc phase is a mixed phase with roughly 50 at% Ag, 27 at% Zn and 23 at% Cu. To draw more precise conclusions about the composition of these phases, as well as their distribution more detailed analytical techniques, such as atom probe tomography, would be necessary.

The fabrication of a ternary alloy consisting of metals with such different reduction potentials (0.7996 V for Ag, 0.3419 V for Cu and -0.7618 V for Zn vs. SHE) [49] is a challenge for ECAM techniques. EHD-RP however, circumvents the difficulty related to preferential de-

position by spatially decoupling the ion reduction from the mass transport. The ejection of the ions is irrespective of the chemical nature and charge of the cations, even for three different metal ions present simultaneously. This advantage could allow EHD-RP to fabricate more complex multi-metal alloys from suitable salt mixtures. To be considered suitable a mixture of salts has to be soluble in the chosen solvent and lead to no precipitation reaction between the salts. An example of a non suitable system would be a mixture containing a Ag salt as well as a chloride salt will lead to the precipitation of AgCl due to its insolubility in water. Therefore, it is important to always utilise compatible salts. If such considerations are taken, the fabrication of further multi-metal alloys should be possible using EHD-RP.

4. Conclusions

We demonstrated the use of aqueous metal salt electrolyte solutions as metal cation precursors for EHD-RP AM. The move away from sacrificial sources and to aqueous electrolytes is expected to significantly broaden the materials range accessible to the method. The overall metal ion concentration was optimised to a concentration of 1 mM to deposit Cu, Ag and Zn structures of high purity. This approach was extended to mixed metal salt solution for the fabrication of Cu-Ag, Cu-Zn and Cu-Ag-Zn alloys. The composition could be precisely controlled across the entire range by tuning the composition of the mixed metal salt solution accordingly. While we have demonstrated only up to three elements in an alloy, there is little reason to assume that more components would pose more significant challenges, as long as salt solubility and compatibility are considered. Similarly, an extension to other elements should be feasible as long as individual metals can be electroplated from aqueous electrolytes. Facile tuning of alloy composition in the future could allow for the fabrication of alloys with optimised properties, for example to improve corrosion resistance (Cu-Ag alloys [51]) or mechanical properties, but also to unlock materials for new applications like thermocouples (Cu-Ni alloys [37]) or actuators (Ni-Ti [63,64]). Increasing the number of elements could enable the fabrication of high entropy alloys (HEA) on the sub-micron scale [38], thereby permitting small-scale AM to access an even broader spectrum of materials properties [65].

CRediT authorship contribution statement

M.N., A.R. and R.S. devised the concept. R.S. and A.R. supervised the project. N.P., M.N. and S.H. performed deposition experiments. N.P., M.N. and M.M. provided SEM analysis. N.P. performed TEM analysis on samples prepared by M.N. and M.M. in FIB-SEM. N.P. and M.N. performed ICP-OES measurements. N.P., M.N., M.M. and R.S. validated the results on a regular basis, while all authors discussed the results. N.P. wrote the original paper draft and visualised the data. All authors reviewed and commented on the draft.

Declaration of competing interest

The authors declare that they have no known competing financial interests or personal relationships that could have appeared to influence the work reported in this paper.

Data availability

Data will be made available on request.

Acknowledgements

This work was funded by Grant no. SNF 200021-188491. Electron-microscopy analysis was performed at ScopeM, the microscopy platform of ETH Zurich. The authors thank Beat Aeschlimann and the Group for Trace Element and Micro Analysis at ETH Zurich for the help with the ICP-OES analysis.

Appendix A. Supplementary material

Supplementary material related to this article can be found online at <https://doi.org/10.1016/j.matdes.2023.112364>.

References

- [1] L. Hirt, A. Reiser, R. Spolenak, T. Zambelli, *Adv. Mater.* 29 (2017) 1604211.
- [2] P. Mishra, S. Sood, M. Pandit, A. Goel, P. Khanna, *Int. J. Res. Appl. Sci. Eng. Technol.* 8 (2020) 956–975.
- [3] X. Sui, J.R. Downing, M.C. Hersam, J. Chen, *Mater. Today* 48 (2021) 135–154.
- [4] A.A. Yazdi, A. Popma, W. Wong, T. Nguyen, Y. Pan, J. Xu, *Microfluid. Nanofluid.* 20 (2016) 50.
- [5] J.-H. Lee, J.P. Singer, E.L. Thomas, *Adv. Mater.* 24 (2012) 4782–4810.
- [6] C.T. Liu, J.H. Zhu, M.P. Brady, C.G. McKamey, L.M. Pike, *Intermetallics* 8 (2000) 1119–1129.
- [7] M.R. Douglass, *IEEE Int. Reliab. Phys. Symp. Proc.* (1998).
- [8] A. Molnár, G.v. Smith, M. Bartok, *Adv. Catal.* 36 (1989) 329–383.
- [9] C. Gong, M.S. Leite, *ACS Photonics* 3 (2016) 507–513.
- [10] R. Spolenak, O. Kraft, E. Arzt, *Microelectron. Reliab.* 38 (1998) 1015–1020.
- [11] A.E. Jakus, S.L. Taylor, N.R. Geisendorfer, D.C. Dunand, R.N. Shah, *Adv. Funct. Mater.* 25 (2015) 6985–6995.
- [12] A. Vyatskikh, S. Delalande, A. Kudo, X. Zhang, C.M. Portela, J.R. Greer, *Nat. Commun.* 9 (2018) 593.
- [13] M. Zenou, Z. Kotler, *Opt. Express* 24 (2016) 1431–1446.
- [14] A. Reiser, L. Koch, K.A. Dunn, T. Matsuura, F. Iwata, O. Fogel, Z. Kotler, N. Zhou, K. Charipar, A. Piqué, P. Rohner, D. Poulikakos, S. Lee, S.K. Seol, I. Utke, C. van Nesselroy, T. Zambelli, J.M. Wheeler, R. Spolenak, *Adv. Funct. Mater.* 30 (2020) 1910491.
- [15] J. Schneider, P. Rohner, D. Thureja, M. Schmid, P. Galliker, D. Poulikakos, *Adv. Funct. Mater.* 26 (2016) 833–840.
- [16] M.A. Saccone, R.A. Gallivan, K. Narita, D.W. Yee, J.R. Greer, *Nature* 612 (2022) 685–690.
- [17] N. Gorodesky, S. Sedghani-Cohen, O. Fogel, M. Altman, G. Cohen-Taguri, Z. Kotler, Z. Zalevsky, *Adv. Eng. Mater.* 24 (2022) 2100952.
- [18] N. Gorodesky, S. Sedghani-Cohen, O. Fogel, A. Silber, M. Tkachev, Z. Kotler, Z. Zalevsky, *Crystals* 11 (2021) 291.
- [19] A. Sahu, I.A. Palani, V. Singh, *Mater. Manuf. Process* 37 (2022) 1310–1319.
- [20] C.L. Kang, Y. Xu, K.L. Yung, W. Chen, *Acad. Manag. Rev.* 591–593 (2012) 1135–1138.
- [21] M. Huth, F. Porrtati, S. Barth, *J. Appl. Phys.* 130 (2021) 170901.
- [22] M. Huth, F. Porrtati, O.V. Dobrovolskiy, *Microelectron. Eng.* 185–186 (2018) 9–28.
- [23] F. Porrtati, E. Begun, M. Winhold, C.H. Schwalb, R. Sachser, A.S. Frangakis, M. Huth, *Nanotechnology* 23 (2012) 185702.
- [24] F. Porrtati, R. Sachser, G.C. Gazzadi, S. Frabboni, M. Huth, *J. Appl. Phys.* 119 (2016) 234306.
- [25] F. Porrtati, M. Pohlitz, J. Müller, S. Barth, F. Biegger, C. Gspan, H. Plank, M. Huth, *Nanotechnology* 26 (2015) 475701.
- [26] M.E.H. Bhuiyan, S. Moreno, C. Wang, M. Minary-Jolandan, *ACS Appl. Mater. Interfaces* 13 (2021) 19271–19281.
- [27] J. Hengsteler, B. Mandal, C. van Nesselroy, G.P.S. Lau, T. Schlotter, T. Zambelli, D. Momotenko, *Nano Lett.* 21 (2021) 9093–9101.
- [28] S. Daryadel, M. Minary-Jolandan, *Mater. Lett.* 280 (2020) 125884.
- [29] J. Hengsteler, G.P.S. Lau, T. Zambelli, D. Momotenko, *Electrochem. Sci. Adv.* (2021) e2100123.
- [30] C. van Nesselroy, C. Shen, T. Zambelli, D. Momotenko, *Addit. Manuf.* 53 (2022) 102718.
- [31] G. Ercolano, C. van Nesselroy, T. Merle, J. Vörös, D. Momotenko, W.W. Koelmans, T. Zambelli, *Micromachines* 11 (2020) 6.
- [32] Y.D. Gamburg, G. Zangari, *Theory and Practice of Metal Electrodeposition*, Springer, 2011.
- [33] Y. Lei, X. Zhang, W. Nie, Y. Zhang, Q. Gao, F. Gao, Z. Li, A. Sun, F. Liu, Y. Cheng, G. Xu, J. Guo, *J. Electrochem. Soc.* 168 (2021) 112507.
- [34] C. Shen, Z. Zhu, D. Zhu, C. van Nesselroy, T. Zambelli, D. Momotenko, *Nanotechnology* 33 (2022) 265301.
- [35] A. Reiser, M. Lindén, P. Rohner, A. Marchand, H. Galinski, A.S. Sologubenko, J.M. Wheeler, R. Zenobi, D. Poulikakos, R. Spolenak, *Nat. Commun.* 10 (2019) 1853.
- [36] J.D. Whitaker, J.B. Nelson, D.T. Schwartz, *J. Micromech. Microeng.* 15 (2005) 1498–1503.
- [37] C. Wang, M.E.H. Bhuiyan, S. Moreno, M. Minary-Jolandan, *ACS Appl. Mater. Interfaces* 12 (2020) 18683–18691.
- [38] M.W. Glasscott, A.D. Pendergast, S. Goines, A.R. Bishop, A.T. Hoang, C. Renault, J.E. Dick, *Nat. Commun.* 10 (2019) 2650.
- [39] M. Nydegger, A. Pruška, H. Galinski, R. Zenobi, A. Reiser, R. Spolenak, *Nanoscale* (2022).
- [40] M. Menétrey, L. Zetzulka, P. Fandré, F. Schmid, R. Spolenak, *arXiv:2308.08323 [physics.flu-dyn]*.
- [41] M. Menétrey, L. Koch, A. Sologubenko, S. Gerstl, R. Spolenak, A. Reiser, *Small* 18 (2022) 2205302.

- [42] Z. Huang, G. Meng, Q. Huang, Y. Yang, C. Zhu, C. Tang, *Adv. Mater.* 22 (2010) 4136–4139.
- [43] M. Ganjian, L. Angeloni, M.J. Mirzaali, K. Modaresifar, C.W. Hagen, M.K. Ghatkesar, P.-L. Hagedoorn, L.E. Fratila-Apachiteia, A.A. Zadpoor, *Nanoscale* 12 (2020) 21988–22001.
- [44] M. Chen, H. Lee, J. Yang, Z. Xu, N. Huang, B.P. Chan, J.T. Kim, *Small* 16 (2020) 1906402.
- [45] P.R. Subramanian, J.H. Perepezko, *J. Phase Equilib.* 14 (1993) 62–75.
- [46] A. Kawecki, T. Knych, E. Sieja-Smaga, A. Mamala, P. Kwasniewski, G. Kiesiewicz, B. Smyrak, A. Pacewicz, *Arch. Metall. Mater.* 57 (2012) 1261–1270.
- [47] M. Kowalski, P.J. Spencer, *J. Phase Equilib.* 14 (1993) 432–438.
- [48] W. Gierlotka, S.-W. Chen, *J. Mater. Res.* 23 (2008) 258–263.
- [49] <https://hbcpc.chemnetbase.com/faces/contents/InteractiveTable.xhtml>, last checked: 24.11.2022.
- [50] Y. Meng, A.J. Bard, *Anal. Chem.* 87 (2015) 3498–3504.
- [51] M. Zenou, A. Sa'ar, Z. Kotler, *Small* 11 (2015) 4082–4089.
- [52] H.-J. Qiu, X.L.L. Pen, H. Xu, Y. Wang, *Corros. Sci.* 92 (2015) 16–31.
- [53] Z. Li, X. Lu, *Bull. Mater. Sci.* 44 (2021) 149.
- [54] R. Ron, E. Haleva, A. Salomon, *Adv. Mater.* 30 (2018) 1706755.
- [55] L. Vegard, *Z. Phys.* 5 (1921) 17–26.
- [56] S. Mader, H. Widmer, F.M. d'Heurle, A.S. Nowick, *Appl. Phys. Lett.* 3 (1963) 201–203.
- [57] J. Song, H. Li, J. Li, S. Wang, S. Zhou, *Appl. Opt.* 41 (2002) 5413–5416.
- [58] R. Bernasconi, J.L. Hart, A.C. Lang, L. Magagnin, L. Nobili, M.L. Taheri, *Electrochim. Acta* 251 (2017) 475–481.
- [59] K.H. Lee, W. Kong, M. Han, D.J. Park, J.H. Ahn, S.Z. Han, Y.-B. Park, K.H. Lee, S. Choe, *J. Alloys Compd.* 881 (2021) 160522.
- [60] S. Strehle, S. Menzel, H. Wendrock, J. Acker, K. Wetzig, *Microelectron. Eng.* 70 (2003) 506–511.
- [61] V.T. Witusiewicz, S.G. Fries, U. Hecht, A. Drevermann, S. Rex, *Int. J. Mater. Res.* 97 (2006) 556–568.
- [62] S.P. Dimitrijević, D. Manasijević, Z. Kamberović, S.B. Dimitrijević, M. Mitrić, M. Gorgievski, S. Mladenović, *J. Mater. Eng. Perform.* 27 (2018) 1570–1579.
- [63] L. Petrini, F. Migliaacca, *J. Metal.* (2011) 501483.
- [64] M.A. Wagner, J.L. Ocana-Pujol, A. Hadian, F. Clemens, R. Spolenak, *Mater. Des.* (2022) 111418.
- [65] E.P. George, D. Raabe, R.O. Ritchie, *Nat. Rev. Mater.* 11 (2019) 515–534.